

Spatial assessment of ~~erosive processes~~ sediment production in a badland catchment using ~~diachronic repeat~~ LiDAR surveys, Draix, Alpes de Haute-Provence, France

Yassine Boukhari¹, Antoine Lucas¹, Caroline Le Bouteiller², Sébastien Klotz², Gabrielle Chabaud¹, and Stéphane Jacquemoud¹

¹Institut de physique du globe de Paris, Université Paris Cité, CNRS, 75005 Paris, France

²Univ. Grenoble Alpes, INRAE, CNRS, IRD, Grenoble INP, IGE, 38000 Grenoble, France

Correspondence: Yassine Boukhari (boukhari@ipgp.fr) and Antoine Lucas (lucas@ipgp.fr)

Abstract. With denudation rates locally exceeding one centimetre of ~~fresh-weathered~~ marl per year, i.e., more than ~~250-200~~ T.ha⁻¹.yr⁻¹, the badlands of the Durance basin in the French Alps are one of the most heavily ~~eroded-eroding~~ areas in the world. ~~The Since 1983, the~~ Draix-Bléone Observatory has been using hydro-sedimentary stations ~~since 1983~~ to monitor several ~~of these~~ small, unmanaged badland catchments, where the hydrological response to seasonal storms is rapid and intense. ~~We combine chronicles from the Laval basin outlet (86 ha) with a six-year diachronic~~ In order to fingerprint soil loss in the 86-ha Laval basin, we combine outlet records with an analysis of airborne and UAV LiDAR data ~~, as well as bulk density modelling taken over a six-year period, alongside a bulk density model and hydrographic network reconstruction. This allows us~~ to map mass movements and ~~constrain a catchment-scale mass balance. We observe~~ determine a sediment budget at catchment scale. ~~We find~~ that landslides and ~~crests failures are highly~~ crest failures represent very active areas, accounting for at least 15% of the watershed's sediment budget throughout the period under study, despite affecting only 1% of the bare surfaces. They contribute to the high erosion rates observed in low-drainage areas, with up to two centimetres of fresh marl ~~eroding-lost~~ per year, 3.5 times the average value on the rest of the bare slopes. Despite certain methodological constraints, our approach ~~is highly promising for quantifying and locating~~ seems very promising at identifying local erosion hotspots, ~~as well as for quantifying their contribution to the sediment budget and~~ assessing sediment transport across ~~critical-zone geomorphological~~ compartments. It could also be adapted to time series and more detailed identification of geomorphic processes in order to monitor the dynamics of ~~badlands-badland~~ catchments in a changing climate.

1

Badlands are highly erosive ~~landforms-landscapes~~ with a dissected, ravine-like morphology that is largely devoid of vegetation (??). They generally develop in semi-arid ~~zones-regions~~ and, to a lesser extent, in humid and sub-humid regions, where the lithology is fragile and highly sensitive to climatic events (??). The Draix ~~badlands~~ Terres Noires, in the southern French Alps, are one such area. They result from successive gullyng phases (??) that began at the end of the Pleistocene and are linked to post-glacial climate changes (??). However, they only took on their current badland form during the Little Ice Age (15th-19th

centuries), as a result of intensive agro-pastoral practices (?). While some hillslopes were reforested at the end of the 19th century (in Le Brusquet catchment, for example), others remain mostly unvegetated and are subject to high erosion rates, such reaching up to one centimetre of weathered marl per year, as in the Laval catchment, where this study was conducted (??)is conducted (??).

Numerous studies have been carried out on these badlands on a plot scale at plot scale (1-100 m²) on bare slopes to analyse the interactions between rainfall, runoff and erosion under controlled conditions, and in particular to describe the hydro-sedimentary processes associated with Hortonian runoff or subsurface infiltration (???). Meanwhile (e.g. ???). In parallel, high-resolution topography (HRT) acquisition methods are becoming more widely available to geomorphologists (???) (e.g. ???). Using a terrestrial laser scanner (TLS), ? were able to observe small hillslope processes such as regolith swelling, crack closure, micro-landslides and the initiation of miniature debris flows (MDFs) at the millimetre scale on such plots. However, it should be noted that analyses of these processes may be biased if the size of the plots is insufficient in relation if the plot scale is too small relative to the average distance travelled by entrained materials transport distance of entrained material, the analysis may be unrepresentative and fail to capture the full contribution of primary sediment sources (???). Consequently, the experiment carried out by ? was reproduced by ? on the 0.13 ha Roubine catchment, which is adjacent to the Laval catchment, allowing . This allowed the seasonal dynamics of erosion to be observed in detail, in a transport-limited erosion regime in winter and in a supply-limited regime in summer. Similar studies were Using dendrochronology to calibrate a slope-erosion relationship alongside a high-resolution topographic reconstruction with UAV LiDAR, ? were also able to produce the first map estimating the spatial distribution of erosion rates in the Laval catchment. Similar studies have been conducted using TLS surveys in the Spanish Central Pyrenees (?). ? also used a time-lapse camera to monitor the evolution of MDFs during flash floods in the Roubine gully, analysing their characteristics and confirming their essential role in sediment transport at the onset of a flood, as well as in the biancane and calantchi badland formations in Italy (?). Apart from these notable exceptions, studies conducted at the catchment scale in the Draix area have generally primarily focused on investigating and modelling the complex relationship between sediment export and climatic variables (?????) or (re)vegetation (????). However, the scaling of erosion mechanisms is highly non-linear erosion mechanisms scale up in a highly nonlinear way with increasing drainage area , due to competing effects between due to the competing effects of increased gully connectivity and increased sediment storage, and as well as a change in slope distribution as the dominant control of the slope distribution that dominates erosive processes (???). For example instance, the Laval catchment (86ha 86ha) and the Roubine catchment (13ha 13ha) are neighbours , sharing with similar environmental conditions and forcings, but yet the Laval sediment flux is dominated by suspended sediment contribution, whereas while the Roubine sediment flux is dominated by bedload contribution (?). To assess the relationship between drainage area and sediment production export, ? analysed 16,571 annual export values at plot and catchment scale from 87 Mediterranean badland sites. They observed a very high and extremely variable sediment production high and highly variable sediment export for drainage areas < 10ha, followed by a power-law decrease in sediment export with drainage area for larger areas. This deviation from the ? model for Mediterranean environments shows that badlands, while seemingly ideal natural laboratories, have a badlands have an intrinsic complexity (?). This result was obtained in configurations with strong vegetation and climatic contrasts and, as well as different monitoring methods, some of which. Some of these methods, such as

gauging stations, are considered more reliable than others ~~that are more widely used~~, such as runoff plots or erosion pins ~~(?)~~. ~~This calls~~, which are more widely used ~~(?)~~. The limitations of the existing sediment yield assessment monitoring methods call for a multi-scale study that ~~integrates, for comparative purposes, several scales within the same catchment, spatially identifies soil loss~~ using a unique ~~measurement method~~, ~~non-invasive measurement method~~ and quantitatively analyses topographic changes.

Airborne remote sensing methods are often used to inventory local sediment sources, ~~assess their volume and discuss their role in the overall erosion of a catchment (???)~~ ~~estimate their volume, and evaluate their contribution to overall catchment erosion (e.g. ????)~~. In the case of landslides ~~(??)~~, this is facilitated by empirical area-volume relationships ~~(????)~~, ~~but also by (e.g. ??????)~~, as well as the advent of photogrammetric methods based on aerial photographs ~~(???)~~ ~~(e.g. ???)~~. More recently, airborne LiDAR systems ~~(????)~~ ~~(e.g. ????)~~ have made it possible to reconstruct the topography of ~~an entire basin~~ ~~entire basins~~ at high resolution ~~, while limiting obstructions by slopes (??)~~. ~~To date, however, such studies estimate while overcoming slope obstructions (???)~~. However, ~~to date, such studies have estimated~~ the volumes of sediment sources and sinks without assessing ~~the corresponding mobilised masses (??)~~ ~~their corresponding masses (???)~~, thus failing to take into account the variations in compaction associated with erosive processes ~~like such as~~ landslides ~~(??)~~. These variations ~~in porosity~~ can be significant, ~~especially particularly~~ in badlands where ~~there is a 1:2 ratio between the ratio of~~ the bulk density of ~~the disaggregated~~ colluvial deposits at the foot of slopes ~~and that of the unweathered marl (?)~~ ~~to that of unweathered marl is 1:2 (?)~~. Furthermore, ~~these approaches usually evaluate topographic changes using Differences of DSMs (DoDs), which are generally less accurate than direct point cloud comparisons in regions with complex terrain (??)~~.

This study aims to ~~fully~~ explore the potential of ~~diachronic LiDAR data to study erosion processes~~ ~~multi-temporal LiDAR surveys to spatially resolve sediment production, defined as the initial mobilisation of weathered material~~, in the Laval experimental basin, ~~where both sediment density and production are measured at a gauging station at its outlet. It also aims to establish a relationship between this process and the sediment export measured at the outlet gauging station~~. Section 2 describes the study area and presents the gauging station ~~and LiDAR data~~, ~~LiDAR data~~, and density measurements. Section 3 describes the procedure for mapping mass movements ~~within the hydrographic network~~ and performing a ~~mass balance at the sediment budget, which is defined as a mass balance for an open system at catchment scale~~. ~~The results examined in~~ ~~Due to the complex topography of the study area, the core of the proposed method is a direct comparison of the 3D point clouds from the LiDAR surveys~~. Sect. 4 ~~highlight the contributions~~ ~~evaluates the contribution~~ of the inventoried sediment sources and sinks to the erosion dynamics of the watershed ~~. The introduction of specific drainage area, and its geomorphological compartments, which are defined based on specific drainage areas (i.e., the drainage area per unit flow width(?), allows us to locate these sources and sinks within the hydrographic network and to calculate sediment production rates at different scales in different critical zone compartments) (?)~~. Finally, Sect. 5 discusses ~~interpretations of these results, estimates production rates in different geomorphological compartments and examines~~ the suitability of ~~our the~~ methodology for assessing badland erosion processes ~~at different scales and presents perspectives for event and seasonal erosion monitoring across spatial and temporal scales in a changing climate~~.

2 Study site and data

2.1 The Draix-Laval experimental basin

2.1.1 ~~Draix-Laval~~The Laval's Terres Noires

The Laval catchment is a marly, torrential watershed ~~of 86 ha, of which spanning 86 ha,~~ more than 60% ~~of which~~ are gullies and ~~bare steep~~ steep, bare slopes (typically $40^{\circ} - 50^{\circ}$), ~~which are~~ characteristic of badlands. ~~It lies between 850 m and 1250 m~~ Located between 850 and 1250 m in the Bléone valley, ~~it lies~~ near the town of Draix and upstream from Digne-les-Bains (~~in the~~ Alpes de Hautes-Provence ~~) region~~ (Fig. 1).

Draix has a Mediterranean mountain climate, with ~~an~~ annual precipitation of ~~about~~ around 900 mm and considerable ~~interannual~~ inter-annual variability (± 200 mm). ~~Harsh~~ The harsh winters are conducive to the ~~weathering by~~ frost-cracking ~~processes~~ weathering of the Jurassic black marls ~~called 'Terres Noires' known as "Terres Noires" (?)~~. Rainfall in spring and autumn is ~~recurrent but not very intense~~ frequent but not intense, with October being the wettest month at an average of over 120 mm. Storms are frequent in late spring and summer. ~~Their paroxysmal intensity, with an average of five major events per year.~~ Their extreme intensity, exceeding 50 mm.h^{-1} over short periods~~(??)~~, is responsible for torrential floods with ~~concentrations up to 800 g/L~~ suspended sediment concentrations of several hundred grams per litre and event-scale sediment export ~~up to several hundreds cubic meters (?) of several hundred cubic metres (???)~~. This results in ~~a very high inter-annual variability in the very high interannual variability in~~ sediment export, reaching about half of the total. On a regional scale, the ~~Terres Noires~~ Terres Noires are responsible for almost 40% of the sediment load of the Durance, ~~although they represent~~ despite representing only 1.2% of its catchment area (?).

2.1.2 Draix-Bléone Critical Zone Observatory

The extreme fragility of the Laval black marls and the surrounding basins make them ideal experimental sites for ~~studying the processes of badlands erosion~~ conducting experiments on the erosive processes of humid badlands. This is why the INRAE (~~Institut national de recherche en sciences et technologies pour l'environnement et l'agriculture~~ French National Research Institute for Agriculture, Food and Environment) has been monitoring these basins since 1983 ~~, and~~ since 2000, as part of the Draix-Bléone Critical Zone Observatory (CZO). ~~The latter joined in~~ In 2015, ~~the latter joined~~ the OZCAR research network (www.ozcar-ri.org), ~~dedicated to the study of the critical zone~~ which is dedicated to studying the critical zone, the near-surface Earth layer extending from groundwater table up to the top of the vegetation canopy.

A hydro-sedimentary station ~~was has been~~ installed upstream of the confluence of the Laval ravine and the Bouinenc, a tributary of the Bléone river ~~-(see Fig. 1)~~. It consists of a ~~rain gauge, tipping bucket rain gauge and~~ a water level sensor ~~for indirect measurement that makes indirect measurements~~ of the flow ~~in the Parshall flume, discharge at 10-second intervals in~~ a Parshall flume. The station is also equipped with automatic water samplers ~~and a turbidimeter to measure the suspended sediment discharge. The~~ that can take samples at intervals of up to one minute, as well as an optical fibre turbidimeter that measures suspended sediment concentrations at 10-second intervals. The typical particle sizes measured are 5 to $20 \mu\text{m}$ (D_{50}).

Table 1. Point cloud characteristics for the 2015 and 2021 airborne LiDAR campaigns ~~for~~, including the whole catchment points and for the ground point subset.

LiDAR Surveys	Number of Points		Point Cloud Density		Typical 3D Distance	
	Catchment	Ground	Catchment	Ground	Catchment	Ground
07/04/2015	111,254,755	42,432,634	98 m ⁻²	44 m ⁻²	6 cm	5 cm
23/06/2021	28,300,873	15,813,801	30 m ⁻²	20 m ⁻²	8 cm	13 cm

and up to 20 to 90 μm (D_{90}). The coarsest materials that make up the bedload are deposited in the 1400 m³ sediment trap, which is emptied once or twice a year. Topographic surveys of ~~this trap are made~~ the trap are conducted after each intense event
 125 ~~allowing us to~~ measure the ~~bedload contribution to~~ contribution of the bedload to the total sediment export. All data from the Laval station, as well as from the other Draix-Bléone catchments, are described in ? and are available in the BDOH database repository (?). Figure 2 summarises the rainfall data recorded between the two LiDAR surveys in April 2015 and June 2021. Approximately 33 intense rainfall events occurred between the two surveys, 25 of which took place between May and August.

2.2 LiDAR campaigns

130 ~~Two LiDAR surveys were used to carry out a high spatial resolution diachronic~~ A high spatial resolution study of the topography of the Laval basin was carried out using two LiDAR surveys between 2015 and 2021. Table 1 summarises the characteristics of the two point clouds.

2.2.1 UAV LiDAR survey (7 April 2015)

An initial survey was carried out on 7 April 2015 as part of ~~a project supported by~~ the OSUG@2020 LabeX supported project
 135 (?). The Laval basin was scanned by the Sintégra company using ~~a an~~ RIEGL LMS-Q680i full-waveform LiDAR system mounted on a UAV helicopter.

The resulting point cloud is certified, georeferenced, and classified ~~between ground and as either ground or~~ above ground. The altimetric accuracy is estimated to be 3 cm ~~from GPS measurements taken on a control surface. The~~, based on 30 GPS measurements acquired over two control surfaces. Although the nominal planimetric accuracy is ~~said to be~~ 20 cm, ~~but~~ the error
 140 is probably ~~less (smaller given that~~ the nominal altimetric accuracy is 10 cm).

2.2.2 Airborne IGN LiDAR HD survey (23 June 2021)

The LiDAR HD programme, led by the ~~IGN (Institut national de l'information géographique et forestière~~ French National Institute of Geographic and Forestry Information (IGN), aims to provide free access to 3D ~~mapping of France (maps of~~ metropolitan France and its overseas departments and territories ~~(excluding French Guiana)~~ with an accuracy of 10 cm
 145 by the end of 2025 (?). ~~The~~ While the entire country is not ~~yet~~ covered by the programme ~~, but yet~~, the Draix Bléone CZO

catchment area was observed on ~~June-23~~ June 2021 at ~~707~~:34 UTC. The LIDAR system is mounted on an aircraft and uses a mirror-tilting-system-tilting mirror to acquire data in bands.

The data is georeferenced in the Lambert 93 coordinate system ~~and cloud segmentation is applied to distinguish ground, vegetation, buildings, etc., with cloud segmentation applied~~ using IGN's myria3D deep learning algorithm ~~(?)~~. ~~The programme specifications indicate a~~ to distinguish between ground, vegetation and buildings (?). According to the programme specifications, the minimum accuracy (RMS) ~~of is~~ is 10 cm for altimetry and 50 cm for planimetry.

3 Method

2.1 ~~Outlet-cumulative sediment export~~ Density measurements

~~The hydro-sedimentary chronicles are available on the website of the observatory (?). From the instantaneous discharge and suspended sediment concentration, and the volumes scoured from the sediment trap, converted to tonnes at the measured density of 1700 kg.m^{-3} (?), we can estimate the total export of sediment M_{tot} at the station. Table 3 summarises the annual and cumulative export between the two LiDAR campaigns, with expanded uncertainties (see Appendix ?? for details). It totals $89.0 \pm 28.6 \text{ kT}$ between April 2015 and June 2021. In the sediment trap, a dry density value of 1.7 g.cm^{-1} is used to estimate the mass of material deposited following a storm event, as determined by topographic surveys (?). However, measurements carried out in 2001 in the Roubine trap, adjacent to the Laval basin, yielded an average value of 1.5 g.cm^{-1} (?). This study repeats the density measurements, this time at various sites in the Laval catchment, primarily in sediment deposits along the channel and its banks, as well as in colluvium at the bottom of slopes and gullies. The experimental protocol is as follows:~~

~~Annual and cumulative sediment export measured at the catchment outlet between the two LiDAR campaigns~~

1. Sampling a sediment deposit using an 11 L bucket;
2. Weighing the sample using a hook balance;
3. Placing 3D-printed reglets around the sample area;
4. Photographing the sample area from different angles;
5. Sampling a portion of the deposit using a vial;
6. Measuring the wet/dry weight before and after 48 hours of oven drying, and determining the initial water content of the sample;
7. Estimating the *in situ* volume of the sample by photogrammetry based on the photographs taken in the field;
8. Calculating the dry density of the deposit from the measured mass, occupied volume and estimated water content χ , with $\rho_{dry} = \rho_{wet} / (1 + \chi)$. ~~$M_{susp.}$ and $M_{dep.}$ are~~

The measurement uncertainties include those related to the ~~cumulative suspended matter and deposited sediment in weight~~ of the sample taken from the 11 L bucket, the volume measurement, and the water content χ . A value of 10% can be assumed for the weight, while the volume uncertainty is typically 100 mL, i.e., about 2% of the ~~sediment trap~~ volume. Consequently, the wet density values are known within an average range of 0.2 g.cm^{-1} . The water content could not be determined for all samples. Values measured in March 2024 ranged from 11.96% to 15.65%, with corresponding reductions in dry density from 86.5% to 89.3%. Where the water content was not measured, a value of $14 \pm 10\%$ was assumed. This gives an average uncertainty in the dry density values of 0.25 g.cm^{-1} . ~~M_{tot} is the sum-~~

Density measurement campaigns were carried out in the sediment deposits of the Draix Laval basin in March and June 2024. In March, the water content of the samples was measured, while in June, a mean value of 14% was used, with an error margin of 10%. Table 2 shows the density measurements according to the geomorphological processes involved. Colluvial deposits have particularly low densities, and landslide material is also significantly less dense than that found in the channel bed or on the riverbanks.

Table 2. Measurements of ~~these contributions~~ dry density using geomorphological processes. ~~2015 and 2021 are marked with a † in the table to indicate that data are reported from 7/04/2015 up to 23/06/2021.~~

Sediment export (kT) Process	2015†201620172018201920202021†Cumulative	Dry density (g.cm^{-1})
M_{susp} Colluvial deposits at the bottom of slopes		12.3 ± 5.4 1.14 ± 0.4
Landslide/Debris avalanches deposits	7.3 ± 2.7 4.3 ± 1.1 13.7 ± 4.5 19.4 ± 8.8 5.3 ± 2.6 2.0 ± 1.0	64.3 ± 26.1 1.41 ± 0.6
M_{dep} Alluvial terraces (surface)	4.1 ± 0.4 3.8 ± 0.4 2.4 ± 0.2 5.5 ± 0.6 4.9 ± 0.5 2.8 ± 0.3 1.2 ± 0.1	24.7 ± 2.5 1.69 ± 0.8
M_{tot} Riverbed deposits (surface)	16.4 ± 5.8 11.1 ± 3.1 6.7 ± 1.3 19.2 ± 5.1 24.3 ± 9.3 8.1 ± 2.8 3.2 ± 1.1	89.0 ± 28.6 1.59 ± 0.8

~~Taking two similar periods, between April 2008 and June 2014 and between April 2012 and June 2018, we obtain in the same way a total sediment export of $87.0 \pm 26.7 \text{ kT}$ and $87.5 \pm 28.8 \text{ kT}$. In the following we consider the former value to be representative of the behaviour of the basin on this timescale, which is long enough to compensate for the large inter-annual variations~~

3 Method

The availability of two high-resolution LiDAR surveys that cover the entire Laval basin alongside hydro-sedimentary records from the outlet and density measurements, provides an opportunity to assess sediment production in a spatially distributed manner. The workflow involves a detailed analysis of topographic changes carried out directly on the 3D point clouds. These are then projected onto a regular grid to estimate the corresponding volumetric changes, which are converted into mass changes using sediment density measurements.

3.1 LiDAR topographic change assessment

The volumetric changes derived from multi-temporal LiDAR surveys are assessed through a three-step process. This process is described below and summarised in Figure 3.

3.1.1 Refinement of the co-registration of the campaigns

Co-registration of LiDAR campaigns is a major source of systematic error, ~~as~~. For example, a shift of one centimetre in the z -axis between point clouds of an ~~86ha catchment will lead~~ 86-ha catchment area will lead to an over- or underestimation of the total volume ~~of by~~ 8600 m³. Systematic ~~co-registration errors~~ errors in co-registration can also occur in the horizontal

200 plane, leading to ridge misalignment. In this study, we refine the point cloud co-registration by analysing the distribution of local ~~distances~~ 3D distances between the campaigns' point clouds on subsets of the catchment area. ~~We focus~~ on nearly stable flat surfaces ~~for vertical errors~~, to identify vertical errors and on slopes with simple geometry ~~for ridge alignment (see Fig. D1)~~ to align ridges. The method used to compute local 3D distances is detailed in Section 2.2.2, and further information on the co-registration is provided in Fig D1. We show that a relative shift of ~~about~~ approximately $(\Delta X, \Delta Y, \Delta Z) = (10, 11, 0.5)$

205 ~~expressed in centimetres~~ cm, of the order of the distance between neighbouring points within a cloud, must be applied to the ~~2015 campaign to perform accurate diachronic~~ 2021 campaign to enable accurate multi-temporal analysis with the ~~2021~~ 2015 campaign. The absolute planimetric and altimetric uncertainties presented in Sect. 2.2 are reduced to $(\delta X, \delta Y, \delta Z) = (\pm 5, \pm 5, \pm 1)$ cm in the relative position between clouds. This also reflects the internal accuracy of the point clouds.

3.2 Diachronic analysis of local volume change210 **3.1.1 Local distances between the point clouds**

The evolution of the topography from one campaign to the next is assessed by calculating the local distances h_{\perp} between the corresponding clouds along the normals to the source surfaces. This is ~~done~~ achieved using the M3C2 (Multiscale Model to Model Cloud Comparison) method, developed by ?, which ~~takes into account~~ considers the local roughness scales of complex natural surfaces. By studying LiDAR data and aerial photographs of the Super-Sauze landslide, ~~in the Ubaye Valley in the~~

215 Alpes de Haute-Provence region, which is also composed of Jurassic black marl, ? have ~~shown~~ demonstrated that this method is an accurate and versatile tool for analysing these active areas, ~~outperforming~~. It outperforms DoD (Difference of DSMs) methods, as well as point-to-point ~~or and~~ point-to-mesh measurements. As the point clouds for the 2015 and 2021 campaigns distinguish ~~vegetation or structures from~~ between vegetation/structures and ground points, only the latter sub-cloud is used ~~in~~ our study for each campaign in our study. Given the complexity of our surfaces and the point densities presented in Table 1, we

220 empirically set the local scale suitable for distance calculation to ~~$r = 30\text{cm}$~~ $r = 30\text{ cm}$ for both clouds. Uncertainties in local distance computation result from the combined standard deviations of surface normal estimation on the source cloud and local distance measurements with the target cloud (?).

~~The mapping of volumetric~~

3.1.2 Inferring local volume changes

225 Volumetric variations in topography ~~is achieved~~ are mapped by rasterising the resulting point cloud to a 1 m^2 grid. This ~~allows~~ enables small mass movements to be captured while ~~taking into account~~ accounting for the density of the point clouds and avoiding empty cells. ~~This gives~~ For each grid cell, rasterisation assigns an average value ~~to the different fields, including for~~ the different attributes, such as height and local distance. ~~From~~ We then construct prisms from this grid, ~~we construct prisms~~ whose volume corresponds to the local variation between the two campaigns: ~~the~~. The surface model is used to orientate
230 the base facets according to the topographic gradient, and the local distance between the point clouds determines their height (~~Appendix B1~~ see Appendix A). The signs of the M3C2 local distances are retained in the volume calculations to indicate whether accumulation or erosion has occurred. Standard deviations ~~can also be~~ are also propagated throughout, ~~allowing~~ enabling us to estimate the volume ~~uncertainties~~ uncertainty of each irregular voxel.

3.2 Effective ~~marl~~ density ~~modelling~~ model of the marls

235 Land movements in the catchment can lead to local and transient accumulations of matter, whereas the integrating nature of the hydrographic network ~~induce that~~ implies that, under the assumption of a steady state, all this matter ~~is ultimately will~~ ultimately be measured at the hydro-sedimentary station. ~~It follows that a mass balance carried out at the scale of the open system constituted by the catchment~~ Consequently, a sediment budget is constructed at the catchment scale, considering it as an open system. It should be closed by the export values measured at the station.

240 ~~In order to establish a watershed mass balance~~

To establish the watershed sediment budget and capture the contributions of different erosion modes, it is essential to map (and sum) changes in mass, δM_{xy} , rather than volume. ~~This is,~~ δV_{xy} . This can be achieved by using local bulk densities, which cannot be measured directly at the catchment scale and are likely to vary considerably ~~with~~ depending on the local material type (e.g., fresh bedrock, regolith, alluvial or colluvial deposits), ~~which~~. It also depends on the local history of ~~seour~~ erosion
245 and deposition. ~~A~~

We have therefore developed a simplified bulk density model ~~, the construction of which is detailed in Appendix ??,~~ ~~has therefore been developed~~ based on sediment ~~deposition~~ deposit measurements and marl weathering profiles from other studies (e.g. ??). Figure 4 shows ~~the effective dry density as a function of the measured local distance between the 2015 and 2021 topographies. The~~. As shown in Sect. 2.1, the dry bulk density of sediment deposits varies considerably due to
250 geomorphological processes. However, for practical purposes, a mean constant value of $1.40 \pm 0.3 \text{ g.cm}^{-3}$ is adopted here. For eroded materials, our model should reflect the marl weathering profile, which varies significantly with depth, as demonstrated by ? and ?. The compact marl horizon is located at a depth of approximately 45 cm with a material density of 2.65 g.cm^{-1} (???). This is overlain by a stratified regolith that is progressively weathered towards the surface, where the density varies seasonally. It reaches a minimum of $(1.39 \pm 0.2) \text{ g.cm}^{-1}$ in winter due to frost-cracking and a maximum of (1.76 ± 0.2)
255 g.cm^{-1} in summer when it is exposed to transport processes during seasonal storms (?). Accordingly, we define a linear density profile of eroded materials with depth, ranging from $1.6 \pm 0.3 \text{ g.cm}^{-1}$ at the surface to $2.65 \pm 0.3 \text{ g.cm}^{-1}$ (not exceeding 2.8 g.cm^{-1}) at 45 cm, beyond which it is assumed to be constant.

Figure 4.a shows the resulting model. In order to incise a layer at a given depth, the upper layers must first be eroded. Thus, at a given local distance h_{\perp} measured between the local surfaces of two surveys corresponds an effective density $\rho_{eff} = \int_0^{h_{\perp}} \rho(z_{\perp}) dz_{\perp}$, shown on Figure 4.b. By construction, the resulting profile is framed by two variations ± 0.3 density-points- g.cm^{-1} at a given depth, which makes it possible to estimate the thus providing an upper and lower bound that estimates the associated extended uncertainties. This-However, this model does not take-into-account-account for the spatial variability of marl deposition and weathering profiles by design.

3.3 Outlet cumulative sediment export

The hydro-sedimentary records are available on the observatory's website (?). From the discharge and suspended sediment concentration, and the volumes scoured from the sediment trap, converted to tonnes at the measured density of 1.7 g.cm^{-1} (?), we can estimate the total sediment export M_{tot} at the station. Table 3 summarises the annual and cumulative export over the sequence, with expanded uncertainties calculated using the quality codes assigned by ?, see Appendix B1 for details. The cumulative export totals $89.0 \pm 28.6 \text{ kT}$ between April 2015 and June 2021.

Table 3. Annual and cumulative sediment export measured at the catchment outlet between the two LiDAR campaigns. $M_{susp.}$ and $M_{dep.}$ are the cumulative suspended matter and deposited sediment in the sediment trap, respectively. M_{tot} is the sum of these contributions. The years 2015 and 2021 are marked with a † in the table to indicate that data are reported from 7/04/2015 up to 23/06/2021. Expanded measurement uncertainties are calculated using quality codes assigned to the recorded date ?, see Appendix B1 for details

Dry-bulk density profile $\rho_{eff}(d_{\perp})$ for weathered marls and sediment deposits as a function of local distance measured between topographies:

Sediment export (kT)	2015†	2016	2017	2018	2019	2020	2021†	Cumulative
$M_{susp.}$	12.3 ± 5.4	7.3 ± 2.7	4.3 ± 1.1	13.7 ± 4.5	19.4 ± 8.8	5.3 ± 2.6	2.0 ± 1.0	64.3 ± 26.1
$M_{dep.}$	4.1 ± 0.4	3.8 ± 0.4	2.4 ± 0.2	5.5 ± 0.6	4.9 ± 0.5	2.8 ± 0.3	1.2 ± 0.1	24.7 ± 2.5
M_{tot}	16.4 ± 5.8	11.1 ± 3.1	6.7 ± 1.3	19.2 ± 5.1	24.3 ± 9.3	8.1 ± 2.8	3.2 ± 1.1	89.0 ± 28.6

By taking two similar periods, between April 2008 and June 2014 and between April 2012 and June 2018, we obtain a total sediment export of $87.0 \pm 26.7 \text{ kT}$ and $87.5 \pm 28.8 \text{ kT}$, respectively. Hereafter, we consider the former value to be representative of the basin's behaviour on this timescale, as it is long enough to compensate for the large inter-annual variations.

3.4 Hydrographic network reconstruction

The following erosion and deposition features will be identified in two ways: by manually labelling sources and sinks and by localising them within the hydrographic network.

The labelling of erosion hotspots, to be discussed in the next section, is primarily carried out on the resulting change map, supported by topographic information and interpretation of orthoimages. Five categories will be defined: crest failures, landslide scars, landslide deposits, a natural dam in the main channel, and the sediment trap at the outlet.

280 To investigate the contributions of each sediment sources and sinks in relation to their location within the basin, we use the GraphFlood algorithm (?) to reconstruct the hydrographic network of the Laval catchment under flood conditions, based on the 50 cm DEM derived from the 2015 LiDAR campaign. This algorithm uses graph theory to efficiently solve the 2D shallow water equations, modelling the characteristics of the flow (e.g., flow rate, water height and flow width) under steady-state conditions for given runoff rates. Here we select a high rate of 50 mm.h^{-1} , which corresponds to intense rainfall likely to generate sediment transport (?). The method enables us to introduce hydro-geomorphic metrics, such as the specific drainage area (also known as the effective drainage area), which is generally constructed as the ratio of the drainage area to the flow width, estimated from contours. Within this algorithm, it is defined as the ratio of the discharge per unit flow width (specific discharge) to the runoff rate (??). This metric is commonly used in hydrological modelling (??) and slope erosion modelling (??), or in combination with slope to define the Topographic Wetness Index (TWI) as a proxy for soil moisture (??). The widespread use of high-resolution digital elevation models, particularly those generated using airborne LiDAR, has made it possible to accurately describe the structure of watercourses and to use this metric, which takes flow width into account (?). Figure 6 presents the resulting map, which is discussed further in the following section.

4 Results

4.1 Mapping of erosion and deposition signals hotspots

295 Figure 5 shows the local mass changes in the denuded areas of the Laval basin. ~~We exclude here vegetated areas, where resulting from the workflow described in Sect. 3.1 and 3.2. Vegetated areas are masked using an orthophotography from IGN (2021), as erosion is assumed to be negligible compared to less significant in these areas than in denuded areas (??) and where surface reconstruction is considered less reliable.~~ Surface reconstruction is also considered to be less reliable in these areas (see Sect. ??). ~~It appears that the mass variations are not evenly~~ 5.2). The mass variations appear to be unevenly distributed across the basin: 97% of the bare areas have values between -1 T/m^2 and $+1 \text{ T/m}^2$ (about $\pm 40 \text{ cm}^{-1} \text{ T.m}^{-2}$ and $+1 \text{ T.m}^{-2}$ (approximately $\pm 40 \text{ cm}$ of fresh marl), but this represents only 54% of the total mass balance on LiDAR sediment budget in denuded areas. This is because significant signals greater than a few T/m^2 T.m^{-2} are found on slopes, in areas limited to a few tens of square metres. Erosion and deposition signals are generally associated, with the latter extending a few metres downstream of the former. These local movements are sometimes visible on orthoimages constructed from aerial photographs, supporting which supports the interpretation of shallow landslides or debris flows. In addition, avalanches. Additionally, when examining the hydrographic network in Figure 6 or the topography in a DEM, it is evident that some of the erosion signals tend to be are located on the ridges of the slopes and are therefore referred to as crest slopes ($< 10^0 \text{ m}^2.\text{m}^{-1}$ specific drainage area) and are consequently categorised as crest or ridge-top failures. Finally, some strong signals strong signals above $\pm 1 \text{ T.m}^{-2}$ are also found in the main drain channel ($> 10^6 \text{ m}^2.\text{m}^{-1}$ specific drainage area), in the sediment trap at the outlet, and 650 m upstream, extending over 200 m. These erosion and deposition hotspots are manually labelled labelled manually in Fig. 5 and 6.

4.2 Contribution of erosion modes Contributions to the sediment production export

Calculating the total ~~mass balance at the catchment scale~~ LiDAR sediment budget at catchment scale $\sum_{xy} \delta M_{xy}$, excluding vegetated areas, ~~we obtain yields~~ an export estimate of 60 ± 20 kT. ~~With the previous assumptions, in particular the choice of a bulk over the 6-year sequence.~~ This uncertainty range reflects the upper- and lower-bound sediment density profiles used in Sect. 3.2, while volume-related uncertainties are minimal, amounting to no more than one kilotonne. Using the central density profile, ~~we are able to explain about the estimated export corresponds to~~ 67% of the sediment export ~~measured-recorded~~ at the outlet, which is ~~of the order of approximately~~ 89 ± 30 kT. ~~Uncertainties are discussed~~ As the two sediment budget values are expected to match, the 23% discrepancy is attributed to measurement uncertainties in the station records, simplified bulk density modelling and, to a lesser extent, limitations of the LiDAR processing workflow, as discussed further in Sect. 4.15.2.

Sediments produced by landslides account for a significant proportion (14%) of the ~~measured-outlet~~ export, but occupy less than 1% (0.8 ha) of the ~~surface area of the basin~~ catchment surface area. However, ~~as 29% of the landslide material remains on the slopes, in average,~~ this proportion falls to 10% ~~if we assume that only 71% of the deposits associated with these landslides are drained on average during the sequence.~~ Similarly, the erosion observed on ~~ridges-ridge tops~~ accounts for 4% of the export ~~covering and covers~~ only 0.2 ha (~~4-four~~ times less than landslides). These estimates ~~could-may~~ be underestimated as there is a 23% discrepancy ~~in the mass balance, which falls within the uncertainty ranges between the sediment budget estimated from records and that estimated from the LiDAR surveys.~~

Figure 5 shows that significant erosive activity ~~is-associated-occurred in association~~ with the ‘La Coulée’ landslide that ~~occurred in December 1998 took place~~ on the left bank of the main channel ~~in December 1998.~~ This structural landslide mobilised ~~between 4500 and 5600~~ $4500-5600$ m³ of compact marl (?), corresponding to 12 to 15 kT. ~~It struck the opposite slope~~ and temporarily obstructed the Laval torrent. ~~According to ? and ?, this landslide, by striking the opposite slope, forced the gradual evacuation of its materials by the torrent. This dynamic-main channel, which gradually evacuated the materials (??).~~ This activity continues as the landslide ~~seems to have generated~~ ~~has generated an additional~~ 2.2 kT of sediment between our two surveys, ~~of which.~~ Of this, 0.7 kT did not reach the main channel and remained on its slopes, ~~as can be seen in Figure 5.~~

The timescale ~~at which we perform the diachronic of the multi-temporal~~ LiDAR analysis is such that Fig. 5 integrates several of the seasonal variations observed in the main channels ~~notably by ???, making the interpretation more difficult. Nonetheless, the strong signal observed,~~ as documented by ?, ? and ?, which complicates the interpretation. Nevertheless, the significant erosion signal (-1.7 ± 0.2 kT) detected in the channel ~~immediately-directly~~ upstream of the landslide ~~suggests-indicates~~ that the obstruction ~~continues to disrupt sediment transport in-is still disrupting sediment transport within~~ the basin. ~~It seems that this obstacle has~~ This obstacle appears to have created a temporary reservoir ~~that,~~ which can be filled under a transport-limited regime or, conversely, erosion regime or emptied under a supply-limited regime.

4.3 Localisation of mass variations within the hydrographic network

~~Map of the specific drainage areas binned in decades. An inventory of the sediment sources and sinks is overlaid.~~

To further investigate the contributions of each class of sediment sources and sinks in relation to their location within the basin, we reconstructed the hydrographic network of the Laval catchment under flood conditions using the 50 cm DEM derived from the 2015 LiDAR campaign and the GraphFlood algorithm (?). The latter efficiently uses graph theory to solve the 2D shallow water equations and thus models the characteristics of the flow (flow rate, water height, flow width) under steady-state conditions for given runoff rates. Here we choose a high rate of about 50 mm/h, corresponding to an intense rainfall that is likely to generate sediment transport. The method allows the introduction of hydro-geomorphic metrics such as the specific drainage area (Fig. 6), sometimes called the effective drainage area, generally constructed as the ratio of the drainage area and the flow width estimated from contours and, within this algorithm, as the ratio of the discharge per unit flow width (specific discharge) and the runoff rate (??). It is commonly used for hydrological (??) and slope erosion modelling (??) or in combination with slope to define the Topographic Wetness Index (TWI) as a proxy for soil moisture (??). The widespread use of high resolution digital elevation models, in particular those generated using airborne LiDAR, has made it possible to accurately describe the structure of watercourses and to use this metric, which takes into account flow width (?). Figure 7.a) Figure 7a shows the distribution of local mass variations due to erosion or deposition as a function of the corresponding specific drainage area, ~~indicating~~. This indicates the sources and sinks ~~that were~~ previously identified in Fig. 5 and 6. A second scale ~~indicates-illustrates~~ the correspondence between the specific drainage area and the upslope contributing area (see Fig. C1).a.

As ~~already mentioned~~, a large ~~mentioned in Sect. 4.1~~, the majority of points correspond to mass changes between -1 T/m^2 and $+1\text{ T/m}^2$ ~~-1 T.m⁻² and +1 T.m⁻²~~ and are distributed ~~over~~ ~~across~~ all drainage areas. However, ~~almost-nearly~~ 50% of the ~~mass-balance comes~~ ~~sediment budget originates~~ from outside this range. Points with higher deposition are mainly concentrated in the specific drainage areas between 10^0 and $10^1 \text{ m}^2/\text{m.m}^2.\text{m}^{-1}$ and to a lesser extent, between 10^1 and $10^4 \text{ m}^2/\text{m.m}^2.\text{m}^{-1}$, mostly corresponding to landslide deposits. Points of higher erosion are mainly concentrated in specific drainage areas below 10^2 and above $10^4 \text{ m}^2/\text{m.m}^2.\text{m}^{-1}$, corresponding respectively to crest ~~and landslide erosion~~, ~~erosion~~, ~~landslide erosion~~ and main channel drainage.

~~By examining~~ ~~Examining~~ the sums of positive (deposition) and negative (erosion) cumulative mass changes for each ~~decade of~~ specific drainage area ~~, it is~~ ~~logarithmic interval makes it~~ possible to determine their ~~weight in the sediment balance~~ ~~contribution to the sediment budget~~, as well as ~~those that~~ of the labelled sediment sources and sinks within them (Fig. 7.b). As some ~~low drainage area signals~~ ~~signals from low drainage areas~~ actually correspond to levees, ~~emerging rocks~~ ~~large boulders~~, floodplains and terraces ~~above the flood level~~ of the main channel and ~~its~~ tributaries, we define a 1m-buffer around gullies and ~~channel~~ ~~channels with a specific drainage density~~ above $10^3 \text{ m}^2/\text{m.m}^2.\text{m}^{-1}$ and a 2m-buffer above $10^4 \text{ m}^2/\text{m.m}^2.\text{m}^{-1}$. This creates another class in Fig. 7.b). ~~By excluding this contribution~~, ~~b. Fig. 6 and 7.b) show that~~ ~~b show that~~, ~~by reassigning this contribution to the channels~~, specific drainage areas feed into each other from ridges to slopes and finally ~~hydrographic network so that we now into the hydrographic network~~. Taking this adjustment into account, we therefore assume that the ~~decades log intervals~~ of specific drainage area may actually reflect ~~critical zone~~ ~~geomorphological~~ compartments that are susceptible to produce and transport sediments with different dynamics:

- The crests typically have submetric specific drainage areas, i.e., upslope contributing areas ranging from 0 to ~~about~~ ~~approximately~~ $1/3 \text{ m}^2$. For ~~this decade~~ ~~these drainage ranges~~, 17% of the ~~mass-balance~~ ~~sediment budget~~ corresponds to

rocks and levees in the channels, 19% to the previously identified crest failures and ~~about-around~~ 9% to landslide scars, ~~the last two together occupying~~. The latter two together occupy around 6% of the ~~surface area of the compartment~~ compartment's surface area. It can be assumed that raindrop splash erosion (???) contributes to diffuse erosion in this compartment (?). As expected, there is almost no accumulation ~~in this compartment and the mass balance totals~~, with the sediment budget totalling 12 kT, i.e., 20% of the overall ~~balance export~~ for less than 7% of the denuded area.

- The "Slopes" compartment ~~slopes~~ are defined by the following two ~~decades-log intervals~~ of specific drainage area ~~and therefore range~~, ranging up to 100 m². Over these ~~decades-log intervals~~, crest failures are negligible but landslide scars account for 16% and 20% ~~respectively of the mass balances of the sediment budget respectively~~, while deposits account for 9% and 17% (2-3% of the corresponding surface areas). ~~For deposition and erosion, most~~ Most of the signals ~~for deposition and erosion~~ are not classified ~~and probably correspond to diffuse processes such as erosion by Hortonian runoff, sheet washing, soil creep or erosion/filling or small rills on slopes~~. Here ~~Once~~ again, up to 17% of the cumulative mass changes over these ~~decades-log intervals~~ correspond to levees and ~~flood plains floodplains~~ belonging to the hydrographic network. Excluding these contributions, the slope compartment accounts for 69% of the overall ~~mass balance sediment budget~~, while occupying 79% of the denuded areas.
- The remaining four ~~decades-log intervals~~ describe the hydrographic network itself, with gullies ~~of~~ up to 10⁴ m² (1 ha) ~~and for the main channel and tributaries above that~~. This is consistent with the ~~considerations made by assumptions made in~~ ? and ?. Compared to the previous compartment, the signal corresponding to the hydrographic network is small, even in the main channel ~~where we identified a~~, where, we identified in Section 4.2 a natural dam upstream of the "La Coulée" landslide (~~4.3-1.7~~ kT), or taking into account the levees, floodplains and terraces (–4 kT). ~~We could have observed a~~ A signal up to 2.4 kT ~~could have been observed~~ coming from the ~~accumulation beach~~ 1400 m³ sediment trap, but this is not the case as it appears at the same filing level between the two campaigns (Fig. 5).

4.4 Production rate calculation for each specific drainage area compartment

5 Discussion

~~Mass balances can be carried out for each compartment or decade of specific drainage areas,~~

5.1 Active mass wasting areas

Our study emphasises the significance of landslide scars and crest failures as erosional hotspots. As estimated in Sect. 4.2, these features contribute around 15% of the basin's sediment budget, despite affecting only 1% of the bare soils. More specifically, they make a significant contribution to the specific drainage areas ranging from metres to tens of metres, accounting for half of the strongest signals exceeding 1 T.m⁻².

As our study covers a period of six years, it is reasonable to assume that these active unstable zones are not necessarily the result of a single slope failure. Instead they may have experienced a succession of smaller movements to clear the debris

410 accumulated downstream due to incision or headwater recession (?). This is particularly evident in the case of the 'La Coulée'
landslide, which continues to experience significant erosive activity two decades after being triggered. Consequently, and
despite the size of these active zones, we believe that our results may be consistent with those of ? and ? on miniature debris
flows (MDF). However, this remains to be examined in detail, as these authors claim that MDFs play a crucial role in the
transport of coarse sediments, contributing between 5 and 36% of the total export of the neighbouring Roubine basin.

415 Finally, our study shows that, on average, 29% of landslide deposits remain on the slopes over the studied period. Supplementing
the time series with other high spatial resolution campaigns, as well as specific event-scale surveys, would enable the drainage
of these materials to be monitored, the geomorphological processes involved to be characterised and, the evolution of these
active areas to be described more generally. While Section 3.3 showed that this six-year sequence provides a representative
record of sediment export, incorporating additional campaigns would further consolidate estimates of sediment export contributions
420 and help determine whether these are characteristic of these badlands.

5.2 Sediment production of the main geomorphological compartments

In Section 4.3, it was observed that the specific drainage area defines hydrologically ordered geomorphological compartments.
Following the adaptation of the landscape partitioning method developed by ? as proposed by ?, which distinguishes convex
hillslopes, unchanneled valleys, and the fluvial domain based on the inflection points of the hydraulic slope-specific drainage
425 area relationship in a log-log diagram, Figure C1.b reveals a relatively good correspondence with the crest, slope, and
hydrographic network compartments (including gullies, channels, and tributaries) that we define here. However, it should be
noted that transitions between hydro-geomorphological domains are not clear-cut, even with this convexity-based partitioning
method. Furthermore, as demonstrated in *calanchi* badlands by ?, this functional relationship is insufficient to accurately
separate geomorphological process domains in such environments, since these processes can operate and interact within the
430 same drainage areas.

Sediment budgets can still be calculated for each compartment, taking into account that they ~~feed into each other~~ are
interconnected and may be subject to transient sediment deposition and drainage, as sediment ~~tend~~ tends to move in pulses
~~aecross~~ across the landscape (?). ~~We should also take into account contributions that have~~ Some areas with low specific
drainage ~~areas, but are actually part of~~ correspond to features such as levees, floodplains or large boulders located in or near the
435 main channel. These areas are therefore reassigned to the hydrographic network, as explained above, compartment, as detailed
in Sect. 4.3.

In order to derive the corresponding production rates, ~~it is necessary to exclude~~ the contributions due to remobilisation
must be excluded. To achieve this, we consider two boundary cases for each compartment, corresponding to the transition
from a transport-limited regime to a supply-limited regime, or vice versa. ~~Indeed, the~~ The first campaign may occur at a time
440 when erosion is transport-limited, ~~such that sediment, resulting in the accumulation of~~ at most the total upstream production,
~~accumulates~~ in a given compartment. These deposits may be drained between the two campaigns, with the second campaign
occurring when erosion is supply-limited. ~~The mass balance~~ Therefore, the sediment budget in this compartment may ~~therefore~~
overestimate the amount of sediment produced inside by ~~as much as up to~~ the total upstream production, which gives us an

initial constraint on maximum sediment production. Subtracting the total upstream production from the sediment budget would then provide a lower-bound estimate of the sediment production in the given compartment. Conversely, the second campaign may have been carried out at a time occurred when the given compartment is/was accumulating material produced upstream ; under transport-limited conditions, whereas the first campaign was occurred in a supply-limited regime. Again, these deposits may represent at most all of what has been the material produced upstream, so that when a diachronic analysis is used to derive erosion rates, the meaning that when erosion rates are derived from a multi-temporal analysis, the sediment production of the compartment may be underestimated by as much. We are probably closer to the former case, which is consistent with the draining of the so-called 'La Coulée' natural dam (Fig. 5) by late spring rainfalls (31/04, 01/05 and 10/05), as the first survey took place in early April 2015 and the second in late June 2021. Adding the upstream production would then provide an upper-bound estimate of the sediment production.

For-

Figure 8 shows a conceptual model of the various compartments found in a badland catchment area. Insets (a) and (b) show two examples of mass movements, with the source areas located in the crest and slope compartments, respectively. An initial LiDAR survey conducted at this stage would capture a transport-limited erosion regime in the slope compartment, as the landslide deposits remain stored on the slopes. A later survey, conducted when the slope compartment is under a supply-limited regime, might measure the remobilisation of these deposits, resulting in a strong erosion signal recorded in both areas. For inset (b), this signal would accurately reflect sediment production in the slope compartment. However, the calculation framework presented here ensures that the erosion signal observed in inset (a) may instead reflect production from the crests. Conversely, if the landslides occurred between the LiDAR surveys and the conceptual model represents the subsequent topography, a change map similar to Fig. 5 would show strong signals originating from the crests in inset (a), which would be accurately reflected in the sediment production of this compartment by the presented method. However, sediment production from the slope compartment would be underestimated due to the presence of deposits. Nevertheless, the proposed method provides a lower-bound estimate for this compartment. Sediment production associated with the landslide in inset (b) would only be accounted for once deposits have been removed from the slope compartment.

In our case study, the production rate for crests not fed from upstream ; the production rate is simply the ratio of the mass balance for a compartment to the sediment budget for the compartment to its corresponding area. We obtain obtained a value of $-42 \text{ kg/m}^2/\text{year}$, i.e., a production rate twice as high as the $-21 \text{ kg/m}^2/\text{year}$ obtained from the export values $42 \text{ kg.m}^{-2}.\text{yr}^{-1}$. This is twice the $21 \pm 7 \text{ kg.m}^{-2}.\text{yr}^{-1}$ export measured at the outlet, integrating the production on all of the denuded slopes of the catchment. For the slopes, the previous approach gives a production rate of between -16 and $-8 \text{ kg/m}^2/\text{year}$, ranging from 16 to $8 \text{ kg.m}^{-2}.\text{yr}^{-1}$ with an indicative value of $-12 \text{ kg/m}^2/\text{year kg.m}^{-2}.\text{yr}^{-1}$, which is already lower than the average value obtained from outlet export, but in line with the $-13 \text{ kg/m}^2/\text{year}$ obtained with the export measured by our diachronic analysis. Again, $14 \pm 5 \text{ kg.m}^{-2}.\text{yr}^{-1}$ obtained with LiDAR sediment budget. As the late spring rainfall events of 2021 (see Fig. 2) appear to have drained the "La Coulée" natural dam, as can be seen in Figure 5, we are likely closer to the former scenario in the hydrographic network. This would mean a transition from a transport-limited regime during the first campaign in early April 2015 and a supply-limited regime during the second campaign in June 2021. This suggests

that sediment production in this compartment is between 0 and 10 kg.m⁻².yr⁻¹, or even between 0 and 8 kg.m⁻².yr⁻¹
under the assumption that the natural dam and the sediment trap solely store upstream materials and do not contribute to
sediment production. However, these values could be underestimated as they remain a, given the 23% discrepancy in the mass
balance. Although our framework could theoretically be applied to gullies and channel tributaries, the resulting uncertainties
are too large to provide a reliable estimate of their production rates. sediment budget between the LiDAR survey estimation
and the measured export. These sediment production estimates from each geomorphological compartment, as well as the
geomorphological processes that can potentially be responsible for these primary sediment productions, are summarized in the
conceptual model illustrated in Fig. 8.

6 Discussion

5.1 Insights across spatial and temporal scales

A characteristic of badlands is the conjunction of sparse vegetation, steep slopes of over 45°, and impermeable marl bedrock
beneath the weathered layer. This favours the initiation of Hortonian runoff between the gullies, which effectively washes away
the altered material produced on the bare slopes in winter (??). In line with the data analysed by ? or ?, and in contrast to other
Mediterranean environments (??), our study shows that the areas producing the most sediment in badlands are those with the
lowest drainage area and the steepest slopes. In this way, we can measure 75% of the export for specific drainage areas smaller
than 10 m².m⁻¹ (approximately two-third of bare areas) and 20% of the export solely for submetric specific drainage areas
(less than 7 % of the bare areas). In accordance with the corrigendum (?) to the study of ?, Fig. 7 shows lower production below
1 m² of upslope contributing area (smaller than the sampling scale) where the slope becomes convex, no longer concentrates
runoff, and is probably characterised only by “splash erosion”. However, as soon as this limit is exceeded, the erosion processes
driven by the steepness of the slope are so efficient that the crests compartment defined above has a production rate twice as
high as that of the rest of the slopes. As confirmed in our study, the predominant influence of slope accounts for the notable
agreement between our erosion map (Figure 5) and that produced by (?), who calibrated a slope–erosion relationship using
dendrochronological data.

Another important driver of erosion is the nature of the substrate, as emphasised by (?). Although the lithology is relatively
homogeneous in the Draix badlands, leading these authors to propose parallel erosion and constant slope angles, our study
challenges this assumption at the considered timescale. Furthermore, heterogeneity in weathering depth across interfluvial
slopes and thalwegs has been reported by ?, (?) and (?), with deeper weathering profiles on ridge tops and shallower ones
in thalwegs. This suggests that, from an *in situ* sediment production perspective, thalwegs operate under a supply-limited
regime. In contrast, ridge tops, despite experiencing higher erosion rates, do not exhibit such limitations. This indicates highly
effective winter weathering processes, likely sustained by the removal of weathered material in summer, which continuously
exposes fresh substrate. This dynamic may also be influenced by the presence of more resistant calcareous layers that are
progressively being exhumed by erosion and which have been observed in thalwegs. This has previously been noted for the
Blue Marls by (?). It is worth noting that such heterogeneity in weathering profiles across ridge tops, slopes and thalwegs may

lead to misestimation of production rates in these compartments. This issue is discussed further in 5.1. Given the feedback loops between topography and erosion, it would also be valuable to consolidate our findings on the distinct evolution of geomorphological compartments over time through long-term monitoring.

The timescale of the study determines the processes to which a multi-temporal analysis can be sensitive. Accumulating data over years makes gradual erosion easier to detect and reliably quantify on the top of slopes that are unlikely to temporarily store sediment, particularly where the terrain is very steep. This also enables mean production rates to be estimated that compensate for inter-annual variability and provide a representative description of the behaviour of the basin over these timescales. Conversely, adapting this method to characterise sediment connectivity in the hydrographic network requires finer temporal resolution to capture the seasonal alternation between transport-limited erosion in winter and supply-limited erosion in summer (??). Alongside finer spatial resolution, we should be able to link large-scale mass movements to climatic forcing. This could improve the modelling of sediment transport during floods and provide insight into hysteresis loops, particularly clockwise loops observed at hydro-sedimentary stations (?), which we suspect may be related to debris flow inputs from slopes or gullies.

5.2 Methodological constraints

To our knowledge, this is the first study to ~~perform a catchment-scale mass balance with~~ combine sediment export measurements at the outlet (89 ± 30 kT) and ~~mapped maps of~~ mass movements over ~~the bare areas of the catchment bare slopes~~ (60 ± 20 kT) ~~to perform a catchment-scale mass balance and determine its sediment budget~~. The performance of this method depends on:

- The quality of the LiDAR time series (point cloud density ~~and~~ accuracy) and its co-registration, assessed over stable zones. The sensitivity of our global ~~balance sediment budget~~ to a z -shift is ~~estimated to be~~ around $10 \text{ kT} \cdot \text{cm}^{-1}$, while our uncertainty on z is estimated to be in the millimetre to centimetre range at most (Fig. D1).
- Reconstitution of local variations in volume. The associated uncertainties ~~result essentially~~ result from the choice of grid cell size, ~~±plus or minus~~ 8 kT, depending on whether a size of $0.5 \text{ m} \times 0.5 \text{ m}$ or $2 \text{ m} \times 2 \text{ m}$ is chosen. The 1 m value limits the number of empty cells for which the value must be interpolated. The other uncertainties propagated in the processing chain ~~are of the order of amount to~~ a few hundred tonnes at most. ~~In addition, the effect of~~ Additionally, rainwater infiltration can ~~also cause the cause~~ regolith to swell or shrink ~~on the millimetre scale (?), which by a few millimetres, as described in (?). This~~ could result in a weak ~~measured signal that signal that is not characterised here and~~ does not correspond to erosion.
- The design of a bulk density model to ~~be associated with the calculated volume variations at each point in the basin convert~~ local volume changes during the sequence into local mass changes. This is the most difficult variable to constrain ~~as,~~ since the spatial and temporal variability of weathering and deposition profiles can significantly alter our estimates of displaced or accumulated mass (???). The density ranges defined in Sect. ~~3.4 give mass balance~~ 3.2 provide sediment budget uncertainty estimates of ± 20 kT, i.e., 7 kT per ~~tenth of a density shift~~ $0.1 \text{ g} \cdot \text{cm}^{-1}$ systematic shift in the density profile shown in Figure 4. Future work could focus on developing bulk density profiles specific to different

geomorphological processes or compartments, as some authors have identified deeper weathering on interfluvies than on
thalwegs (??). This approach would be particularly relevant, given that neglecting this aspect leads to an overestimation
of production on crests and an underestimation of production in thalwegs.

- Measurement uncertainties at the outlet, both in terms of suspension and deposition in the sediment trap. They mainly
reflect the difficulty of calibrating turbidity measurements to estimate suspended matter at low concentrations, as explained
detailed in Table B1 (?). They and the data paper by ?. These uncertainties range within ± 30 kT over the period.

Our work has been carried out on bare badland formations, excluding vegetated areas which, as these are likely to have a
very different weathering profile compared to the proposed that proposed by the density model. In any case, although while
they may be the site sites of deposition or transport, it is expected that material flow will material flow is expected to be low due
to soil fixation by the root system roots (????). In addition Additionally, the density of LiDAR points classified as ‘ground’
is lower under vegetation, making it more difficult which makes it more challenging to reconstruct the topography on such of
surfaces that may be littered with plant leaves or shrubs shrubs.

Finally, in this study, the this study carries out an inventory of sediment sources and sinks is carried out manually using a GIS
tool, with which has limitations in terms of contour delineation and detection thresholds (?). An alternative, although approach,
which is also subject to problems of merging and underdetection problems (??), could be based on supervised or unsupervised
clustering (?). This would be similar to the methods used for landslide detection using, which use pixel-based approaches
(?), object-oriented approaches (??) or deep learning (??) approaches. Our results suggest that the specific drainage area
or the Topographic Wetness Index (?) are good feature candidates, alongside the classical approaches (?). A more detailed
characterisation of the geomorphological processes at play could be achieved by analysing hydro-geomorphological metrics
(e.g., elevation, curvature, slope, flow direction).

5.3 Spatial and temporal scales

A characteristic of the badlands is the conjunction of sparse vegetation, particularly grasses and shrubs to consolidate the
regolith with their root networks, the predominance of steep slopes, exceeding 45° , and the impermeability of the marls that
form the bedrock beneath the weathered layer. This favours the emergence of Hortonian runoff between the gullies, which
effectively washes away the altered material produced in winter on the bare slopes (?). Therefore, in line with the data
analysed by ?, and in contrast to other Mediterranean environments (?), our study shows that the areas producing the most
sediment in badlands are those with the lowest drainage area and the steepest slopes. In this way, we are able to measure 75%
of the export for specific drainage areas smaller than $10 \text{ m}^2/\text{m}$ (about 2/3 of bare areas) and 20% of the export solely for
submetric specific drainage areas (less than 7 % of the bare areas). In accordance with the corrigendum (?) to the study of ?
; Fig. 7 shows lower production below 1 m^2 of upslope contributing area (smaller than the sampling scale) where the slope
becomes convex, no longer concentrates runoff, and is only characterised by “splash erosion” (impact of raindrops on the
weathered regolith). That said, as soon as this limit is exceeded, the efficiency of the erosion processes is such that the crests
compartment defined above has a production rate twice as high as that of the slopes.

The timescale of the study also determines the processes to which such a diachronic analysis can be sensitive. The accumulation of signal over several years makes it easier to detect and reliably quantify gradual erosion on slopes that are unlikely to store sediment temporarily, particularly where the terrain is very steep. It also makes it possible to estimate mean production rates that compensate for inter-annual variability and provide a representative description of the behaviour of the basin on these timescales. Conversely, adapting this method to characterise sediment connectivity in the hydrographic network requires a finer temporal resolution to capture seasonal alternations between a transport-limited erosion regime in winter and a supply-limited regime in summer (??). Together with finer spatial resolution, we should be able to link large mass movements to climatic forcing at the event scale. This could help to better constrain the modelling of sediment transport during floods and to provide explanatory elements for the hysteresis loops, especially clockwise loops observed at hydro-sediment stations (?), which we suspect may be related to debris flow inputs from slopes or gullies.

5.3 Active mass wasting areas

Our study highlights the importance of landslide scars and crest failures as erosional hotspots. As explained in Sect. 4.2, they contribute to about 15% of the sediment budget of the basin, even though they affect only 1% of the bare soils. More specifically, they make a large contribution to the metric to decametric specific drainage areas, and are responsible for half of the strongest signals exceeding 1 T/m^2 metrics in more detail, using approaches such as the MaGPiE algorithm, which was developed specifically for badlands (??).

As our study covers a period of about 6 years, it is reasonable to assume that these active unstable zones are not necessarily the result of a single slope failure, but may have experienced a succession of smaller movements, in particular to clear debris accumulated downstream by incision or headwater recession (?). This is particularly the case for the ‘La Coulée’ landslide, which is still experiencing significant erosive activity two decades after it was triggered. Consequently, and despite the size of these active zones, we believe that our results correlate well with those of ? and ? on miniature debris flows (MDF). These authors claim that they play a crucial role in the transport of coarse sediments, contributing between 5 and 36% of the total export of the neighbouring Roubine basin (?).

Finally, our study shows that an average of 29% of landslide deposits remain on the slopes during the period. Supplementing the time series with other campaigns at high spatial resolution, as well as with specific surveys at the event scale, would make it possible to monitor the drainage of these materials, characterise the processes involved and, more generally, describe the evolution of these active areas.

5.3 Opportunities in a changing climate

Mediterranean environments are among the regions most affected by climate change, ~~with a projected~~. They are projected to experience a significant decrease in precipitation (except in winter ~~for in~~ the southern French Alps), as well as an increase in temperature and ~~an increase~~ in the frequency of paroxysmal events (?). ~~It is therefore~~ Therefore, it is crucial to assess the impact of these changes on the future evolution of critical zone processes, particularly ~~for in~~ vulnerable environments such as ~~the~~ badlands, which ~~are a major contributor~~ contribute significantly to sediment export (?). ~~How~~ It is unclear how their erosive

dynamics, which are closely linked to ~~those of vegetation~~ vegetation dynamics (?), will evolve ~~with in the context of~~ a decrease in winter weathering caused by cryoclastic forcing (?), and a decrease in summer precipitation competing with an increase in the number and intensity of summer storms ~~triggering landslides (??), is still controversial (??) that trigger landslides (???)~~.

However, the widespread availability of high-resolution data is paving the way for the development of geomorphological
615 analysis tools ~~capable of quantifying and spatialising that can quantify and spatialize~~ sediment sources and sinks. The methodology developed in this study offers new prospects for analysing erosion and sediment transport at different scales within a catchment. It ~~represents a promising complement to~~ complements existing observation methods ~~, which could help better constrain and could help to improve the accuracy of~~ hydro-sedimentary transport models ~~that already accurately~~, which already simulate runoff response to precipitation forcing in these catchments ~~, but which have a more accurately, but have~~ limited predictive
620 ability for sediment fluxes (????).

6 Conclusion

We ~~combined a diachronic~~ analysed erosion in a small badland catchment by combining a six-year analysis of LiDAR data ~~acquired at 6-year interval~~ with a material bulk density model ~~to analyse erosion in a small badland catchment. We were able to evaluate~~. This enabled us to calculate a total mass loss of 60 ± 20 kT, ~~corresponding equivalent~~ to an annual erosion rate of 200
625 $T \cdot ha^{-1} \cdot yr^{-1}$ ~~on denuded areas, which is in denuded areas. This represents a 23% less than discrepancy compared to~~ the export measured at the long-term outlet hydro-sedimentary station. ~~We found~~, which is likely due to measurement uncertainties and density modelling. Our findings indicate that landslides and ridge failures are ~~important significant~~ contributors to the total ~~flux sediment export~~ (15% of the total ~~flux export~~ for 1% of the total surface ~~), and that the low area~~). Furthermore, low specific drainage areas are the most productive (20% of the total erosion for 7% of the total surface ~~area~~), while the channel
630 network appears to be primarily driven by the remobilisation of sediments produced upstream. Our method appears to be a ~~very~~ promising approach for assessing sediment transport in badlands ~~under in~~ a changing climate.

. Hydro-sedimentary chronicle data are available on the BDOH database repository (<https://bdoh.inrae.fr/DRAIX/>, ?). The 2015 LiDAR point cloud is available with the following DOI : <https://doi.org/10.57745/DAEB1Z> (?). The LiDAR HD database is available online at <https://geoservices.ign.fr/lidarhd> (?).

635 . YB drove the science, the LiDAR processing chain and produced the results. AL initiated the research. CL and SK provided data and expertise that support this research. GC 3D-printed the reglets used in the density measurements. YB, AL, CL, SJ contributed to writing the paper and sharing ideas.

. The contact author has declared that none of the authors have any competing interests.

. The authors acknowledge the support of the CNES (APR STERREO), the Programme National de Télédétection Spatiale (PNTS, Grant
640 PNTS-2022) and the LabEx UnivEarthS (ANR-10- LABX-0023 and ANR-18-IDEX-0001). This study was carried out at the Draix–Bléone
Observatory (France), using infrastructure and data. The Draix–Bléone Observatory is funded by the INRAE (National Research Institute
for Agriculture, Food and Environment), the INSU (National Institute of Sciences of the Universe) and the OSUG (Grenoble Observatory
of Sciences of the Universe) and is part of OZCAR, the French network of critical zone observatories, which is supported by the French
Ministry of Research and French research institutes and universities. [We thank two anonymous referees and the handling editor for their](#)
645 [constructive reviews that greatly improved the manuscript.](#)

Appendix A: ~~Calculation~~ [Rasterization](#) of local volume changes from cloud-to-cloud distances

The M3C2 algorithm (?) [presented in Sect. 3.1.1](#) is used to evaluate the local distances between two point clouds. A Geotiff
raster with a resolution of 1 m^2 pixels is constructed using 5 scalar fields:

- the average distance between clouds in each cell h_{\perp} ;
- 650 – the corresponding uncertainty value dh_{\perp} ;
- the cell point population p ;
- the mean point height z ;
- the uncertainty on this height value dz .

The surface model is then used to derive the gradient components in the X and Y directions of the grid. The population of each
655 cell is information that can be used to filter cells if, for example, an outlier value is suspected. To calculate the area intercepted
by each mesh in the grid, the grid is locally modelled by a plane whose inclination (θ_x, θ_y) is given by the components of the
gradient in the X and Y directions. The same assumptions are made as for the shallow water equations (see Sect. 4.3), namely
that the choice of grid size causes the length scale for the curvature of the topography to be much larger than the length scale
at which normal variations h_{\perp} are considered. Considering one quadrant of each facet and the plane equation:

$$660 \quad \begin{cases} \text{OA}' = (d, 0, d \times \tan \theta_x) \\ \text{OB}' = (0, d, d \times \tan \theta_y) \end{cases} \implies \text{A}'\text{B}' = d \times (-1, 1, \tan \theta_y - \tan \theta_x)$$

$$\exists n \mid \text{O}', \text{A}', \text{B}', \text{C}' \text{ satisfy } n_x x + n_y y + n_z z = 0$$

$$\implies x \tan \theta_x + y \tan \theta_y - z = 0$$

$$\implies \text{OC}' = d \times (1, 1, \tan \theta_x + \tan \theta_y)$$

665 This gives the area $\mathcal{S}_{\text{OA}'\text{B}'\text{C}'}$ of each facet quadrant as half the product of the diagonals:

$$\mathcal{S}_{\text{OA}'\text{B}'\text{C}'} = \frac{d^2}{2} \sqrt{(2 + (\tan \theta_x + \tan \theta_y)^2)} \sqrt{(2 + (\tan \theta_x - \tan \theta_y)^2)}$$

Voxels can be formed in each cell: the third dimension is given by the M3C2 distance and their volume corresponds to the local erosion/deposition value:

$$\mathcal{V}_{voxel} = 4 \times \mathcal{S}_{OA'B'C'} \times h_{\perp}$$

670 Note that the sign of \mathcal{V}_{voxel} is given by the sign convention for h_{\perp} , which allows us to distinguish erosion values from deposition values. Uncertainties can also be applied to the volume calculation:

$$d\mathcal{V} = h_{\perp} (\partial_{\theta_x} \mathcal{S} d\theta_x + \partial_{\theta_y} \mathcal{S} d\theta_y) + \mathcal{S}_{OA'B'C'} dh_{\perp}$$

where dh_{\perp} is one of the scalar fields contained in the Geotiff frame, as well as dz_{x+1} , dz_{x-1} , dz_{y-1} , and dz_{y+1} , which allows $d\theta_x$ and $d\theta_y$ to be calculated. The barycentre of each cell itself has a positional uncertainty in the plane which is also taken into
675 account by the cell population p .

Appendix B: ~~Construction of the bulk density model~~ Focus on uncertainties in hydro-sedimentary chronicle data

B1 ~~Density of sediment deposits~~

~~In the deposition beach, the dry density value used in the data evaluation is 1.7 (?). However, measurements carried out in 2001 in the Roubine trap, an elementary gully adjacent to the Laval basin, gave a lower average value of 1.5 (?). In this work, density measurements were carried out at various sites in the Laval catchment, mainly in sediment deposits along the channel and its banks, and in colluvium at the bottom of slopes and gullies. The experimental protocol was as follows~~ In Sect. 3.1 we present the cumulative sediment export of suspended M_{susp} and deposited M_{dep} sediments at the outlet of the watershed calculated with:

~~Sampling a sediment deposit using a shovel and an 11 L bucket; Weighing the sample using a hook balance; Placing 3D-printed reglets around the sample area; Photographing the sample area in different orientations; Sampling a portion of the deposit using a vial; Wet/dry weight measuring before/after 48h oven drying and determining of the initial water content of the sample; Estimating the in situ volume of the sample by photogrammetry, based on the photographs taken in the field; Calculating the dry density of the deposit from the measured mass, the occupied volume and the estimated water content~~

$$d_{dry} = d_{wet} / (1 + \chi)$$

$$\begin{cases} M_{susp.} = \sum_t C_{susp.}(t) \times Q(t) \\ M_{dep.} = \sum_t V_{dep.}(t) \times \rho_{trap} \end{cases}$$

where C_{susp} and Q are the concentration of suspended sediments (kg.m^{-3}) and water discharge ($\text{m}^3.\text{s}^{-1}$), respectively, and V_{dep} and ρ_{trap} correspond to the deposited volume in the sediment trap (m^3) and its associated dry bulk density (kg.m^{-3}). The value used for dry bulk density is $\rho_{trap} = 1700 \text{ kg.m}^{-3}$

The measurement uncertainties include those related to the weight of the sample taken from the 11-L bucket, those related to the volume measurement and those related to the water content χ . A value of 10% of the weight can be assumed, while the volume uncertainty is typically 100 mL, i.e., about 2% of the volume. As a result, the wet density values are known within an average range of 0.2. The water content could not be determined for all samples. The values measured in March 2024 ranged from 11.96 to 15.65, with the corresponding dry density reduced from 86.5% to 89.3%. Where this water content was not measured, a value of $14 \pm 10\%$ was assumed. This gives an average uncertainty on the dry density values of 0.25.

Density measurement campaigns were carried out in March 2024 and June 2024 in the sediment deposits of the Draix-Laval basin. In March, the water content of the samples was measured, while in June the mean value of 14% was used with an error of 10%. Table 2 shows the density measurements according to the geomorphological processes involved. It can be seen that scree slopes have particularly low densities, and that landslide or debris flows are also significantly less dense than deposits in the bed or in alluvial terraces.

Density measurements according to geomorphological processes: Process Dry density Scree slope apron at the bottom of the slope 1.14 ± 0.4 Colluvium at the bottom of landslides 1.41 ± 0.6 Alluvial terrace (surface) 1.69 ± 0.8 Alluvial stock in the riverbed (surface) 1.59 ± 0.9

A systematic survey of the densities in these different compartments, as well as a common measurement of the water content of the samples taken, would allow this preliminary study to be carried out in greater depth. A mean value of 1.40 ± 0.3 seems to cover the different types of sediments in the catchment with the same effective density.

B1 Density of eroded materials

A study carried out over 2.5 years by ? in the Moulin basin, adjacent to the Laval basin, measured the effective densities and water content of the surface layer (0-2.5 cm deep) of marl subject to weathering and erosion, and determined how these change over the seasons. It appears that dry density is minimal in late winter (1.39 ± 0.2) and early spring (1.55 ± 0.2), when the slopes have developed an upper layer of weathering, and minimal in late summer (1.76 ± 0.2) and autumn (1.71 ± 0.3), when this layer has been washed by seasonal storms. The average value of 1.61 ± 0.2 emerges. ? used the value of 1.3 to describe the erosion rate of weathered marl, typically around 11–15 mm.yr^{-1} at Laval, based on the ratio of sediment production at the outlet to the area of bare land. Using the value of 1.39 (?) at the end of winter, i.e., when the eroded material is made available on the slopes, this result can be re-evaluated at 10–14 mm.yr^{-1} . If we now consider the production values in Table 3, we find an equivalent ablation value for weathered marl of 18-20 mm.yr^{-1} at the surface, with strong inter-annual variation. As a result, we can estimate the expected average depth of denudation of the slopes in the 2015-2021 interseason at no more than 9-12 cm, i.e. the average thickness of this detrital layer on the slopes according to the study carried out by ?. This means that between these two campaigns, the entire detrital layer present in 2015 has been purged. We choose 1.60 ± 0.3 for the density of this surface layer. Locally, we can also expect the outermost layer of regolith, which was just weathered during the first campaign,

725 to be ground down. It is somewhat harder and denser, but a priori less so than the less weathered or intact marl between 2.1 and 2.65 (???). The above study by ? estimates this horizon of unaltered marl to be about 45 cm deep.

B1 Marl density profiles

730 The considerations from the previous two subsections allow the construction of a simplified density profile model, constant with depth at 1.4 ± 0.3 for sedimentary deposits and linear from 1.6 ± 0.3 at the surface to 2.65 ± 0.3 (not exceeding 2.8) at 45 cm (then constant). To incise a layer at a given depth, the upper layers must first be eroded. Thus, at a local distance d measured between the local surfaces of two surveys, one is sensitive to an effective density ρ_{eff} (Fig. 4), which takes into account the erosion of the overlying layers $M_{loc} = \rho_{eff} \times S \times d = \int_0^d \rho(z) \times S \times dz$. This is the physical quantity used in Sect. 3.4.

Appendix C: Focus on uncertainties in hydro-sedimentary chronicle data

735 In Sect. 3.1 we present the cumulative sediment export of suspended and deposited sediments at the outlet of the watershed calculated with:-

$$\begin{cases} M_{susp.} = \sum_t C_{MES}(t) \times Q(t) \\ M_{dep.} = \sum_t V_{deposit}(t) \times 1.7 \end{cases}$$

740 In the In the data paper of ?, the characterisation of measurement uncertainties is presented in the form of quality codes assigned during the expertise of the data (Table B1). When no quality codes are attributed we assume an intermediate quality, as at that time poor quality data were classified as missing data. There are no data entries flagged as 'low quality' in these datasets, although this may occur for rainfall data for instance. Without further assumptions on their distribution, they are considered as expanded uncertainties propagated by the following equations:

$$\begin{cases} \Delta \left(\sum_i X_i \right) = \sum_i \Delta(X_i) \\ \frac{\Delta(\prod_i X_i)}{\prod_i X_i} = \sum_i \frac{\Delta(X_i)}{X_i} \end{cases}$$

Table B1. Correlation between hydro-sedimentary data quality codes and their corresponding uncertainties~~in hydro-sedimentary data~~, adapted from ?.

Code	1 : No quality attributed	2 : Good quality	3 : Intermediate quality
$Q \text{ (m}^3\text{.s}^{-1}\text{)}$	30% (assumption of this study)	10% (no issues noted)	30% (flooded gauging system or deposit trap full of sediments)
$C_{susp.} \text{ (g.L}^{-1}\text{)}$	60 % for $C_{susp.} < 50 \text{ g.L}^{-1}$ <u>$C_{susp.} < 50 \text{ g.L}^{-1}$</u> and 13% for $C_{susp.} > 50 \text{ g.L}^{-1}$ <u>$C_{susp.} > 50 \text{ g.L}^{-1}$</u>	10% (event-scale calibration)	60% for $C_{susp.} < 50 \text{ g.L}^{-1}$ <u>$C_{susp.} < 50 \text{ g.L}^{-1}$</u> and 13% for $C_{susp.} > 50 \text{ g.L}^{-1}$ <u>$C_{susp.} > 50 \text{ g.L}^{-1}$</u> (inter annual turbidity calibration)
$V_{depos.} \text{ (m}^3\text{)}$	10% (subsidence of drying material)		

Copernicus_LaTeX_Package/fig01.png

Figure 1. Map showing (a) the extent of the "Terres Noires" in the French Alps, represented by hatching (adapted from ?), and (b) the Laval basin, located 1.5 km northeast of Draix, with its hydrographic network and vegetation cover shown in green. (c) Catchment outlet with the sediment trap and hydro-sedimentary monitoring station. (d) Detail of the instrumentation used at the monitoring station. Examples of geomorphological processes observed on the crests (e), slopes (f), and gullies (g) are also presented.

Copernicus_LaTeX_Package/fig02.png

Figure 2. The monthly cumulative precipitation (mm) and 5-min average rainfall intensity (mm.h^{-1}) recorded at the meteorological stations in the Laval basin between 2015 and 2021.

Copernicus_LaTeX_Package/fig03.png

Figure 3. [Workflow for assessing volumetric changes of the topography using point cloud data.](#)

Copernicus_LaTeX_Package/fig04.png

Figure 4. (a) Designed density model $\rho(z_{\perp})$ and corresponding (b) bulk density profile $\rho_{eff}(h_{\perp})$ as functions of weathered marl erosion depth ($z_{\perp} < 0$) or sediment deposits depth ($z_{\perp} > 0$), and local distance measured between topographies (h_{\perp}), respectively. Densities are expressed in g.cm^{-3} .

Copernicus_LaTeX_Package/fig05.png

Figure 5. Local Map of local erosion (in red) and deposition (in blue) mapping over the Laval catchment (French Alps) between the 2015 and 2021 LiDAR surveys over the Laval catchment (French Alps). Vegetated areas are have been masked by using an orthophotography (Institut Géographique National, 2021). An inventory of the sediment sources and sinks is also has been overlaid.

Copernicus_LaTeX_Package/fig06.png

Figure 6. Map of the specific drainage areas, binned in logarithmic intervals and computed with the Graphflood algorithm (?), assuming a runoff rate of 50 mm.h^{-1} and based on a 50 cm-resolution DEM derived from the 2015 LiDAR survey. An inventory of the sediment sources and sinks has been overlaid.

Copernicus_LaTeX_Package/fig07.png

Figure 7. (a) Distribution of local mass variations as a function of the associated specific drainage area (left plot) at any point in the denuded regions, (right plot) cumulated in each decade-log interval of the specific drainage area. The sediment sources and sinks identified above are shown in the same colours as above. Contributions from suspected-levees, emerging-rocks-large boulders and floodplains with a small drainage area but belonging that belong to the hydrographic network area are also shown in gray.

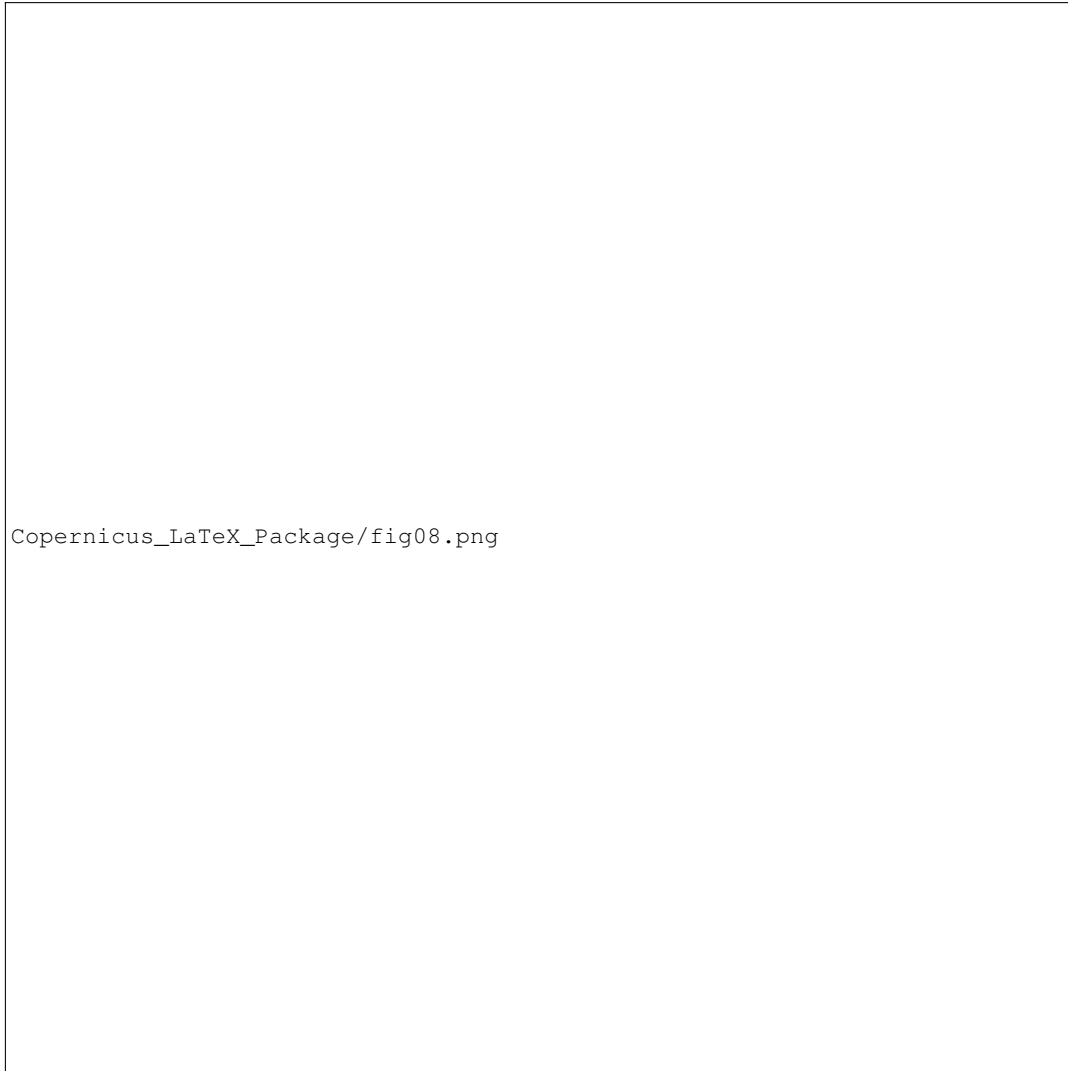


Figure 8. Conceptual model of sediment production across the main geomorphological compartments of a badland catchment. Levees, large boulders and floodplains with a small drainage area that belong to the hydrographic network area are also represented with hatching. Boxes (a) and (b) depict two mass movements, with the source areas located in the crest and slope compartments, respectively, and downslope deposits. The figure also illustrates some of the processes that are potentially responsible for primary sediment production. Schematic adapted from ?



Figure A1. Geometry used to calculate the area of oriented facets describing local surface depletion or accumulation.

Copernicus_LaTeX_Package/figC01.png

Figure C1. (a) Specific drainage area ($\text{m}^2/\text{mm}^2 \cdot \text{m}^{-1}$) against upslope contributing area (m^2) for a runoff rate of $50 \text{ mm/h} \cdot \text{mm} \cdot \text{h}^{-1}$. (b) 2D histogram showing hydraulic slope as a function of specific drainage area. White dots indicate average values within logarithmic bins of specific drainage area. Solid vertical lines delineate geomorphological domains with the inflection point method, while the dashed vertical line marks this study's definition of the crest, slope, and hydrographic network compartments.



Figure D1. (a) Location of the study areas used to characterise the effect of a centimetric co-registration error between two campaigns. Background: Aerial photograph of the outlet of the Draix-Laval basin (IGN, 2021). (b) Distribution of local distances between ground points of the 2021 campaign and the 2015 campaign on the study areas with or without a $(\Delta X, \Delta Y, \Delta Z) = (10, 11, 0.5)$ corrective shift (in centimetres) of the 2021 point cloud.